Materials & Design 247 (2024) 113396

Contents lists available at ScienceDirect

Materials & Design

journal homepage: www.elsevier.com/locate/matdes

Nanostructure-induced functional combination of vanishing magnetostriction and magnetic softness in ferromagnetic $(GaNi)_xCoCrFe$ (x = 0.4–1.6) high-entropy alloys

Jože Luzar [a], Andreja Jelen [a], Juraj Nálepka [b], Saeid Salari [b], Primož Koželj [a,c], Stanislav Vrtnik [a,c], Peter Mihor [a], Julia Petrović [a], Magdalena Wencka [a,d], Goran Dražić [e], Anton Meden [f], Pavol Priputen [b,*], Janez Dolinšek [a,c,*]

[a] Jožef Stefan Institute, Jamova 39, SI-1000 Ljubljana, Slovenia
[b] Slovak University of Technology in Bratislava, Faculty of Materials Science and Technology in Trnava, Jána Bottu 25, SK-91724 Trnava, Slovak Republic
[c] University of Ljubljana, Faculty of Mathematics and Physics, Jadranska 19, SI-1000 Ljubljana, Slovenia
[d] Institute of Molecular Physics, Polish Academy of Sciences, Smoluchowskiego 17, PL-60-179 Poznań, Poland
[e] National Institute of Chemistry, Department of Materials Chemistry, Hajdrihova 19, SI-1000 Ljubljana, Slovenia
[f] University of Ljubljana, Faculty of Chemistry and Chemical Technology, Večna pot 113, SI-1000 Ljubljana, Slovenia

ARTICLE INFO

Keywords:
High-entropy alloys
Multi-scale structured materials
Magnetostriction
Magnetic softness
Nanomagnetism

ABSTRACT

Searching for high-entropy alloys with functional properties that emerge from their multi-scale structure, we have investigated the $(GaNi)_xCoCrFe$ (x = 0.4–1.6) system. We have characterized structure, microstructure, nanostructure and chemical composition of the individual phases in the multi-phase alloys and determined their magnetic, magnetostrictive and electrical properties. We found that the alloys are ferromagnetic and exhibit functional combination of magnetic softness and vanishing magnetostriction, classifying them as energy-efficient "supersilent" materials (inaudible to a human ear) for alternating-current (AC) electromagnetic applications in the audio-frequency range. The alloys develop a two-phase structure, a face-centered cubic (fcc) and a body-centered cubic (bcc), where the fcc phase fraction decreases, while the bcc fraction increases with the increasing $(GaNi)_x$ content. Ferromagnetism of the alloys originates from the highly nanostructured bcc phase, with the ferromagnetic Curie temperatures in the range T_C = 750–700 K, depending on x. The fcc phase is not nanostructured and is paramagnetic at room temperature, but undergoes a spin glass transition at $T_f \approx 6.4$ K. The magnetic softness and vanishing magnetostriction of the alloys are both nanomagnetic phenomena. The magnetic-softness and magnetostriction parameters of the x = 1.3 and 1.6 alloys make them relevant for supersilent AC applications at low frequencies.

1. Introduction

Multi-phase high-entropy alloys (HEAs), sometimes called second-generation HEAs or compositionally complex alloys (CCAs) [1], are metallic alloys composed of more than one solid solution or appear as a mixture of a solid solution and an intermetallic compound (one or more). Beside the academic interest in their formation and stability, multi-phase HEAs are also interesting from the application point of view in relation to their mechanical and physical properties, as they sometimes show enhanced properties or combinations of these that are not present in single-phase materials, either conventional or HEAs. An example of such "smart" mechanical property is a combination of strength and ductility, which are mutually exclusive in single-phase materials. In a two-phase HEA, one phase may possess strength and the other is ductile, overcoming the strength-ductility trade-off [2]. Multi-phase structures also yield interesting magnetic properties, like soft ferromagnetism in nanostructured HEAs containing magnetic elements. This phenomenon has been experimentally and theoretically elaborated in detail for the equiatomic CoFeNiPdCu HEA [3], where the CoFeNi ferromagnetic (FM) clusters of 2–5 nm cross dimensions are

* Corresponding authors at: Jožef Stefan Institute, Jamova 39, SI-1000 Ljubljana, Slovenia (J. Dolinšek), and Slovak University of Technology in Bratislava, Faculty of Materials Science and Technology in Trnava, Jána Bottu 25, SK-91724 Trnava, Slovak Republic (P. Priputen).
E-mail addresses: pavol.priputen@stuba.sk (P. Priputen), jani.dolinsek@ijs.si (J. Dolinšek).

https://doi.org/10.1016/j.matdes.2024.113396
Received 10 September 2024; Received in revised form 11 October 2024; Accepted 20 October 2024
Available online 22 October 2024

randomly intermixed with nonmagnetic PdCu "nano-spacers" of the same size. Magnetic softness is here a nanomagnetic effect. The CoFeNi FM clusters of that smallness are magnetically single-domain particles, and since the particles with randomly oriented FM axes are exchange-coupled across the boundaries, exchange averaging of magnetic anisotropy to zero takes place [4], resulting in excellent magnetic softness, comparable to the best commercial soft magnets. The magnetic softness phenomenon based on the same physical principle was also observed in the three-phase HEAs $AlCoFeNiCu_x$ ($x = 0.6$–3.0) [5], where one phase (highly enriched in Cu) is nonmagnetic, while the other two phases are both CoFeNi-rich and hence FM, but exhibit differently strong ferromagnetism due to different addition of the nonmagnetic elements Al and Cu. By changing the Cu content x in the $AlCoFeNiCu_x$ alloys, the fractions of the three phases and their domain sizes can be adjusted to yield the best magnetically soft performance. The magnetostriction of these HEAs can also be adjusted by changing the Cu content. Magnetostriction is a phenomenon that FM materials change their size and shape in an external magnetic field. When exposed to a periodic magnetization-demagnetization cycling in an alternating-current (AC) magnetic field at audio frequencies (20 Hz–100 kHz), a magnetostrictive material mechanically vibrates and emits humming noise that can be annoying to a human ear (e.g., a humming grid transformer) [6–8]. For the $AlCoFeNiCu_x$ ($x = 0.6$–3.0) HEAs it was shown that the two present FM phases possess magnetostrictive strains of opposite sign that compensate each other in the three-phase composite [5]. Adjusting their volume fractions by changing the Cu content drives the average magnetostrictive strain of the material from positive to negative, yielding precisely zero magnetostriction at a particular Cu content x (in that case at the composition $AlCoFeNiCu_{2.0}$). Such magnetically soft and zero-magnetostriction HEAs classify as "supersilent" materials (inaudible to a human ear) for audio-frequency AC electromagnetic applications and are suitable for the fabrication of supersilent transformer cores, magnetocaloric refrigerators and other humming electromagnetic machinery. Another advantage of the zero-magnetostriction material is that it is not mechanically stressed in an AC magnetic field, which beneficially reduces the mechanic fatigue of the material in the AC device.

Aluminum has been a major alloying element in most HEAs containing magnetic 3*d* transition metals (in addition to the FM Co, Fe and Ni also the antiferromagnetic (AFM) Cr and Mn), because it imparts strength and good oxidation resistance [9]. Possessing large negative binary mixing enthalpies with the magnetic 3*d* elements [10], Al promotes formation of multi-phase structures. In that context, it is interesting to explore the possibility of replacing Al by gallium (Ga), another element from the group 13 of the periodic system. Ga is from the valence-electrons point of view isoelectronic to Al, making the 3+ state the most common oxidation state for both elements. Like the Al metal, Ga metal is also not reactive with air and water at room temperature (RT), because it forms a thin protective passivation oxide layer at the surface, so that the oxidation resistance of the alloys upon Al substitution by Ga is expected to be preserved. Ga possesses large negative binary mixing enthalpies with the magnetic 3*d* elements Ni and Co [10], again promoting multi-phase structures. An advantage of Ga over Al is its smaller atomic radius (r(Ga) = 1.24 Å, as compared to r(Al) = 1.43 Å), which is about the same as the radii of the magnetic 3*d* elements (all about 1.25 Å) [10]. The lattice distortion will consequently be significantly smaller by replacing Al by Ga in this group of HEAs.

The use of Ga as an alloying element in HEAs based on the magnetic 3*d* transition elements has been so far scarce. Ga has been employed in the nanocrystalline HEAs $CoCrFeNiGa_x$, both equiatomic ($x = 1.0$) and non-equiatomic ($x = 0.5$), prepared by spark plasma sintering of powders produced by high energy ball milling [11], and in equiatomic CoCrFeNiGa HEA prepared by arc melting [12]. In a search for multi-phase HEAs within the Co-Cr-Fe-Ni-Ga system with functional magnetic properties, we are reporting here on a series of $(GaNi)_xCoCrFe$ ($x = 0.4$, 0.7, 1.0, 1.3 and 1.6, where $(GaNi)_x$ stands for Ga_xNi_x) alloys prepared by induction melting, where the Ga content has been changed systematically and simultaneously with the Ni content, since these two elements experience the strongest bonding tendency between the elements involved (the binary mixing enthalpy $\Delta H_{mix}^{GaNi} = -15$ kJ mol^{-1} is the most negative of all elemental pairs [10,13], as evident from Table S1 of the Supplementary material). It is considered that the phase formation in HEAs is predominantly governed by the binary constituent pair that evolves first, and this binary pair then determines the parent structure of the alloy, in which other elements dissolve. In the $(GaNi)_xCoCrFe$ HEAs, the first-to-bind binary pair is GaNi, which crystallizes in a B2 structure (a chemically ordered bcc), so that changing simultaneously the Ga and Ni contents adjusts the fraction of the elements that are expected to determine the parent structure of the alloys. We present the evolution of the structure, microstructure, nanostructure and physical (magnetic, magnetostrictive and electrical) properties of the alloys upon increasing $(GaNi)_x$ content and demonstrate that these HEAs are multi-phase soft ferromagnets with near-zero magnetostriction, adding to the class of supersilent materials for the audio-frequency AC applications.

2. Materials and methods

Properties of the elements constituting the $(GaNi)_xCoCrFe$ HEAs are collected in Table 1. The atomic radii of all five elements are about the same, r = 1.24–1.26 Å [10]. The high-temperature (HT) structure of pure Cr and Fe metals is body centered cubic (bcc), while the Co and Ni metals are face centered cubic (fcc). Ga metal has no HT structure because of its low melting point. Upon cooling, Cr (bcc) and Ni (fcc) retain their structures down to RT, while Co transforms at 700 K to a hexagonal close-packed (hcp), which is then its RT structure. The Fe metal first transforms from bcc to fcc at 1665 K, followed by another allotropic transition at 1184 K from fcc back to bcc, which is then retained down to RT. Ga metal is orthorhombic at RT.

The $(GaNi)_xCoCrFe$ ($x = 0.4$, 0.7, 1.0, 1.3 and 1.6) alloys were prepared by induction melting. Before the melting process, the elements with a purity of at least 99.95 % were put in an alumina crucible and placed inside a silica tube. The tube was then mounted on an apparatus that was connected to a device enabling repeated vacuuming and filling with argon. Subsequently, the apparatus was sealed at a pressure of 1 bar to maintain a protective argon atmosphere inside the tube and then disconnected from the device. To melt and mix the pure elements inductively, the tube was inserted into the induction coil. After the melting process, the melt was spontaneously cooled to RT. The resulting samples took the form of cylinders with a diameter of 8 mm and a height of about 20 mm. In the following we shall designate the alloys according to their nominal $(GaNi)_x$ content (e.g., $x = 0.4$, $x = 0.7$,…).

X-ray diffraction (XRD) experiments were performed on powder samples in reflection mode with Fe-filtered cobalt Co $K\alpha_{1,2}$ radiation. A PANalytical Empyrean X-ray diffractometer equipped with a PIXcel3D X-ray detector was used for the experiments. The 2θ range was from 20 to 140° with a step of 0.026°. The measurement time per step was about 500 s. For each investigated alloy, the measurement was repeated five times, and the data were averaged, yielding a high signal-to-noise ratio.

Scanning electron microscopy backscattered-electron (SEM-BSE) imaging and energy dispersive X-ray spectroscopy (EDS) chemical composition determination and elemental mapping were performed by the scanning electron microscopes JEOL JSM-7600F Schottky FE SEM equipped with INCA Oxford 350 EDS SDD and ThermoFisher Quanta 650 ESEM equipped with EDS Oxford Instruments AZtec Live, Ultim Max SDD 40 mm^2.

High-angle annular dark field (HAADF) and bright-field (BF) scanning transmission electron microscopy (STEM) images, STEM-EDS elemental maps and elemental concentration line profiles were obtained by a Cs-corrected Jeol ARM 200 CF STEM microscope equipped with an SDD Jeol Centurio energy-dispersive X-ray spectrometer. The

Table 1
Properties of the elements (by increasing atomic number) constituting the $(GaNi)_xCoCrFe$ alloys (atomic radius r [10], melting temperature T_m, room-temperature (RT) structure with lattice parameters and high-temperature (HT) structure [13]).

Element	$_{24}$Cr	$_{26}$Fe	$_{27}$Co	$_{28}$Ni	$_{31}$Ga
r(Å)	1.25	1.26	1.25	1.25	1.24
T_m(K)	2180	1809	1768	1726	302.9
RT structure	bcc	bcc	hcp	fcc	orthorhombic
a(Å)	2.884	2.866	2.506	3.524	4.519
b(Å)					7.658
c(Å)			4.073		4.526
HT structure	same as RT	bcc (1665 K < T < 1809 K) fcc (1184 K < T < 1665 K)	fcc (700 K < T < 1768 K)	same as RT	

operating voltage was set to 200 kV. The lamellae for the STEM investigations were prepared by the focused ion beam (FIB) Helios NanoLab 650 FEI dual-beam system using gallium ions. Based on the previous experience of FIB sample preparation of Ga-free alloys and metals, a noticeable increase of Ga concentration due to the Ga ion implantation during the FIB thinning process is only in the top Pt protective layer.

Magnetic measurements were conducted on a Quantum Design MPMS3 SQUID magnetometer equipped with a 7-T magnet, operating at temperatures between 1.8 and 1000 K. The samples for measurements were needle-shaped, with the long dimension of 5 mm and the perpendicular dimension of 0.4 mm. The long dimension was set into the direction of the external magnetic field to minimize the demagnetization effects.

Electrical resistivity measurements were performed on a Quantum Design Physical Property Measurement System PPMS 9 T. Rectangular-bar samples of dimensions $1 \times 1 \times 8$ mm^3 were used.

Magnetostriction measurements were performed on thin plates of dimensions $20 \times 5 \times 1$ mm^3 that were cut from cylindrical ingots. The strain gage technique was employed, using the strain gage sensors KYOWA (Japan), model KFNB-2-350-D20-11, gage factors (23 °C, 50 %) (1) 1.81 and (2) 1.95 ± 2.0 %, gage length 2 mm, gage resistance (23 °C, 50 %) 350.0 Ω ± 0.6 %. The gages were glued to the samples with the KYOWA CC-33A adhesive. The samples were oriented along the magnetic field to minimize the demagnetization effects. Superconducting magnet of the PPMS 9T apparatus was used to provide the magnetic field. To increase the sensitivity while measuring the magnetostriction, a Wheatstone bridge was constructed on the PPMS puck out of the strain gage and three high-precision 350.0 Ω resistors. The data from the Wheatstone bridge was measured with the PPMS Resistivity option.

3. Results

3.1. X-ray diffraction phase identification and quantification

The alloys' structures were determined by XRD on powdered samples, using cobalt Co Kα_1 radiation ($\lambda = 1.78896$ Å). The XRD patterns of all five alloys are shown in Fig. 1. An evolution of the structure is observed upon increasing the $(GaNi)_x$ content. For the alloy with the lowest $x = 0.4$ (the topmost trace in Fig. 1), the structure is single-phase fcc. Though the measurements were performed on a powdered sample, the intensities of the reflections did not match well the theoretical powder intensities, indicating some preferential orientation of the microcrystallites (the powdering procedure was not fine enough). In addition, the shapes of some reflections indicate the presence of stacking faults, whereas the reflections from differently oriented crystal planes show different widths (anisotropic broadening), indicating different degrees of crystallinity/periodicity in different crystallographic directions. These features were present for all investigated alloys. The Le Bail fitting procedure (refining the unit cell based on the positions of the reflections and adjusting the intensities individually to fit best) has yielded the fcc unit cell parameter $a = 3.6105$ Å, while an attempt with the Rietveld analysis (refining the unit cell based on the positions of the reflections, while their intensities are bound by the structure factors and

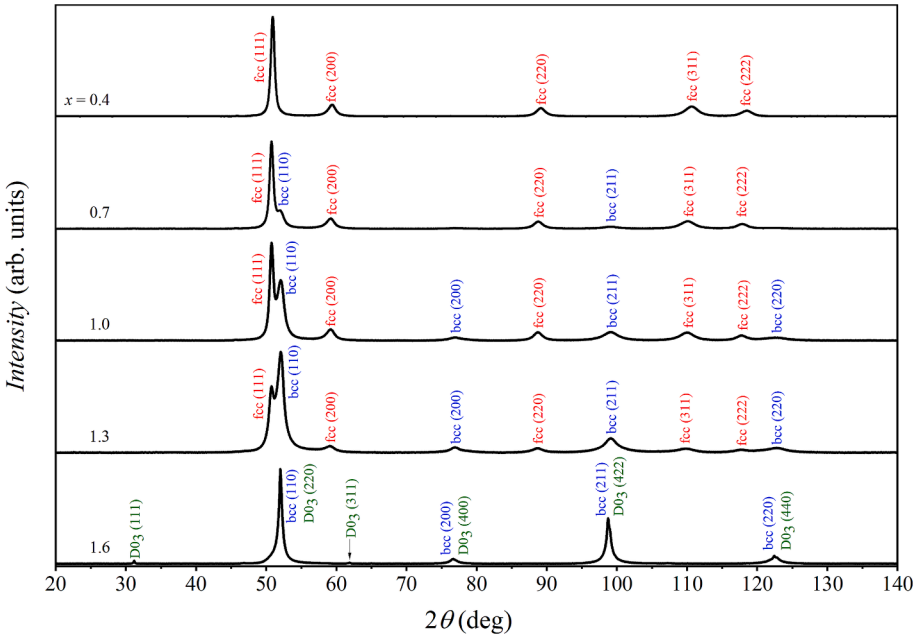

Fig. 1. XRD powder patterns of the $(GaNi)_xCoCrFe$ ($x = 0.4$, 0.7, 1.0, 1.3 and 1.6) alloys at RT.

a refined scale factor) has yielded almost the same result $a = 3.6106$ Å. The phase type and the value of the unit cell parameter (obtained by the Le Bail method) are also given in Table 2. The Le Bail and Rietveld analyses were performed for all five alloys (not shown), but the discrepancy of the unit cell parameters obtained by the two methods were very small in all cases (about the same as that for the $x = 0.4$ alloy), so that in the following we give the results obtained by the Le Bail method.

For the alloys $x = 0.7$, 1.0 and 1.3, the XRD patterns reveal a two-phase structure, an fcc (the same as in the $x = 0.4$ alloy) of a fraction that decreases systematically with increasing x and a bcc of a fraction that increases with x. The fcc unit cell parameter remained about the same in all alloys (no monotonous systematic increase or decrease with x can be claimed, see Table 2), and the same holds for the bcc cell parameter that amounts to $a = 2.8885$ Å for the $x = 0.7$ alloy (Table 2). Quantitative evolution of the fcc and bcc phase fractions (in wt.%) with x is presented in Table 2 and is also shown graphically in Fig. 2a.

For the $x = 1.6$ alloy, the reflections of the fcc phase are no more visible and the XRD pattern could be indexed to the bcc phase with $a = 2.8922$ Å. Careful inspection of the reflections at high diffraction angles reveals their doublet structure, which is due to the presence of the Co $K\alpha_2$ component in the radiation that has not been completely eliminated by filtering (a quite usual experimental situation). The $K\alpha_1$–$K\alpha_2$ splitting is not visible for other alloys due to broader reflections, indicating that the $x = 1.6$ alloy is the best crystallized of all. Moreover, additional reflections of low intensity have appeared at $2\theta = 31.1$ and 61.8°, which are not present in other alloys and could not be indexed to the bcc phase. The analysis has revealed that the second phase is $D0_3$, a cubic phase with a twice-larger unit cell parameter. $D0_3$ is a chemically ordered phase with the A_3B stoichiometry (Fe_3Si-type), where the unit cell is a 2 × 2 × 2 block of the bcc cells (Fig. 2b). The element A occupies all sites that were forming before the vertices of the individual bcc cells (sites α), as well as one half of the sites that were forming before the centers of the bcc cells (sites β, distributed tetrahedrally on the inner (dashed) cube in Fig. 2b). The element B then occupies the other half of the sites from the centers of the bcc cells (sites γ). The $D0_3$ phase is more long-range ordered than the B2 phase (a chemically ordered bcc, FeGa-type). It is worth mentioning that in the case where the sites α, β and γ would be occupied by three different types of elements A, B and C, respectively, this gives the stoichiometry A_2BC and the resulting phase type is L21.

The bcc and $D0_3$ phases with the unit cell parameter a in the ratio 1:2 share several common XRD reflections, i.e., the bcc reflections 110, 200, 211 and 220 overlap with the $D0_3$ reflections 220, 400, 422 and 440, respectively (full lists of the reflections for the two phases are given in the Supplementary material). The reflections at $2\theta = 31.1$ and 61.8° in the XRD pattern of the $x = 1.6$ alloy (the bottommost trace in Fig. 1) belong to the $D0_3$ phase only (these are the 111 and 311 reflections) and prove the coexistence of the bcc and $D0_3$ phases in this alloy. The Le Bail analysis has yielded the unit cell parameters $D0_3$ $a = 5.7755$ Å and bcc $a = 2.8922$ Å, with their ratio 1.997 (the Rietveld analysis has yielded almost identical values, $D0_3$ $a = 5.7731$ Å, bcc $a = 2.8891$ Å and the ratio 1.998). A Rietveld-method estimate of the mass fractions of the two phases based on the theoretical powder intensities indicates that the ratio of the bcc-to-$D0_3$ phases is roughly 2.5:1. In view of the fact that the alloy $x = 1.6$ contains the largest $(GaNi)_x$ fraction of all alloys, and the binary mixing enthalpy of Ga and Ni is the most negative of all elemental pairs in the investigated Co-Cr-Fe-Ni-Ga system, it is reasonable to assume that Ga and Ni at larger concentrations start to build regions of the more long-range chemically ordered $D0_3$ phase (an intermetallic compound of the Ga_3Ni type, but may contain also other elements), whereas the matrix is a chemically disordered bcc solid solution (still to be verified by EDS, presented in the following). The $D0_3$ phase may be present in smaller amount already in the $x = 1.3$ alloy, but the $D0_3$-specific reflections (1 1 1 and 3 1 1) are too weak in intensity and below the detection limit of the powder XRD method.

3.2. Microstructure determination by SEM-BSE imaging

The microstructure of the alloys on the 100-μm scale, determined by SEM-BSE imaging, is presented in Fig. 3. The BSE images show atomic-number (Z) contrast, where the phases enriched in heavier elements (larger Z) appear brighter. The elements constituting the $(GaNi)_xCoCrFe$ HEAs possess the following atomic numbers: Cr ($Z = 24$), Fe ($Z = 26$), Co ($Z = 27$), Ni ($Z = 28$) and Ga ($Z = 31$). The BSE image of the $x = 0.4$ alloy is presented in Fig. 3a, revealing dendritic structure on a 100-μm scale with dark centers and light boundaries of the dendrites. Some even darker minor interdendritic regions, of up to 20-μm dimensions, can also be noticed, while the black holes are pores. The light boundaries are enriched in the heaviest element Ga (or in the two heaviest elements Ga and Ni, to be verified by EDS), while the darker interdendritic regions are enriched in the lightest element (Cr). Upon increasing the $(GaNi)_x$ content, the BSE images of the alloys $x = 0.7$, $x = 1.0$ and $x = 1.3$ show a two-phase structure of a light matrix and dark islands (Fig. 3b–d), where the fraction of the matrix increases, while the fraction of the islands decreases with increasing x. A comparison with the XRD spectra from Fig. 1 indicates that the dark phase is fcc, while the light phase is bcc. The BSE image of the $x = 1.6$ alloy (Fig. 3f) reveals a mixture of two light phases.

The XRD pattern of the $x = 0.4$ alloy shows single phase (fcc) only, whereas its BSE image shows more constituents, the dendrites with dark centers and light boundaries and the even darker minor interdendritic regions. It is realistic to consider that all constituents have fcc structure. The dendrites are formed via the effect known as coring, which results from the solute redistribution during dendritic solidification. The center of each dendrite, which is the first part to freeze, is rich in the high-melting elements (in this case Co, Cr and Fe), whereas the concentration of the low-melting elements (Ni and Ga) increases with position from the center to the dendrite boundary. In this process, the structure of the entire dendrite (the core and the boundary) remains fcc. The mechanism producing the minor interdendritic regions is less clear, but based on the XRD, their structure is also fcc.

Table 2
List of the investigated $(GaNi)_xCoCrFe$ alloys, their chemical compositions, structure, crystallographic parameters and weight fractions of the constituent phases. The column "Appearance" describes morphologic appearance of the phase in the multi-phase microstructure (in relation to Fig. 3).

Alloy	Nominal average composition (at.%)	Appearance	SEM-EDS composition	XRD structure	Fraction (wt.%)
$(GaNi)_{0.4}CoCrFe$	$Ga_{10.5}Ni_{10.5}Co_{26.3}Cr_{26.3}Fe_{26.3}$	dendrite interior (darker)	$Ga_{8.9}Ni_{9.8}Co_{26.9}Cr_{26.8}Fe_{27.6}$	fcc, $a = 3.6105$ Å	>98
		dendrite boundary (lighter)	$Ga_{17.5}Ni_{16.7}Co_{22.6}Cr_{22.9}Fe_{20.3}$	fcc	?
		dark interdendritic	$Ga_{17.1}Ni_{10.4}Co_{20.4}Cr_{31.7}Fe_{20.4}$	fcc	?
$(GaNi)_{0.7}CoCrFe$	$Ga_{15.9}Ni_{15.9}Co_{22.7}Cr_{22.7}Fe_{22.7}$	dark islands	$Ga_{12.3}Ni_{13.7}Co_{24.3}Cr_{24.3}Fe_{25.4}$	fcc, $a = 3.6226$ Å	77
		light matrix	$Ga_{23.7}Ni_{20.0}Co_{19.2}Cr_{19.4}Fe_{17.7}$	bcc, $a = 2.8885$ Å	23
$(GaNi)_{1.0}CoCrFe$	$Ga_{20.0}Ni_{20.0}Co_{20.0}Cr_{20.0}Fe_{20.0}$	dark islands	$Ga_{15.0}Ni_{16.8}Co_{22.2}Cr_{22.5}Fe_{23.5}$	fcc, $a = 3.6225$ Å	44
		light matrix	$Ga_{24.2}Ni_{21.9}Co_{18.1}Cr_{18.4}Fe_{17.4}$	bcc, $a = 2.8877$ Å	56
$(GaNi)_{1.3}CoCrFe$	$Ga_{23.2}Ni_{23.2}Co_{17.9}Cr_{17.9}Fe_{17.9}$	dark islands	$Ga_{16.6}Ni_{19.1}Co_{20.7}Cr_{21.4}Fe_{22.2}$	fcc, $a = 3.6137$ Å	24
		light matrix	$Ga_{25.0}Ni_{24.2}Co_{17.0}Cr_{17.1}Fe_{16.7}$	bcc, $a = 2.8814$ Å	76
$(GaNi)_{1.6}CoCrFe$	$Ga_{25.8}Ni_{25.8}Co_{16.1}Cr_{16.1}Fe_{16.1}$	lighter	$Ga_{27.2}Ni_{27.5}Co_{15.2}Cr_{15.0}Fe_{15.1}$	$D0_3$, $a = 5.7755$ Å	29
		darker	$Ga_{24.5}Ni_{23.8}Co_{16.8}Cr_{17.6}Fe_{17.3}$	bcc, $a = 2.8922$ Å	71

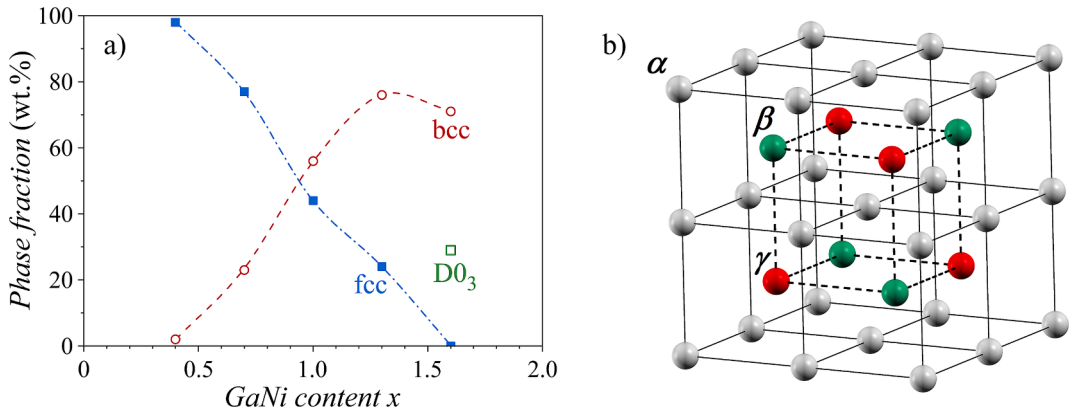

Fig. 2. (a) Weight fractions of the fcc, bcc and $D0_3$ phases in the $(GaNi)_xCoCrFe$ alloys as a function of the $(GaNi)_x$ content. (b) Unit cell of the $D0_3$ phase.

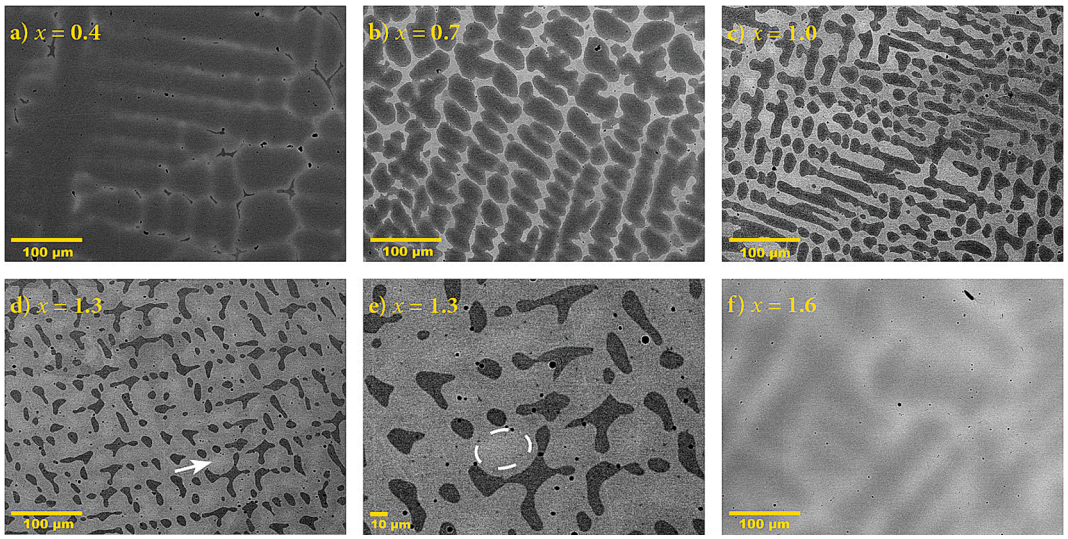

Fig. 3. SEM-BSE images of the $(GaNi)_xCoCrFe$ ($x = 0.4$, 0.7, 1.0, 1.3 and 1.6) alloys. The panel (e) shows an expanded region of the panel (d) (the BSE image of the $x = 1.3$ alloy), with one slightly brighter region (a $D0_3$ precipitate) within the bcc matrix encircled. The position of the encircled region in the panel (d) is indicated by an arrow.

The BSE image of the $x = 1.6$ alloy presented in Fig. 3f reveals the coexistence of two phases, with the majority phase appearing slightly darker than the brighter minority phase. Since the XRD pattern of the $x = 1.6$ alloy no more shows the reflections of the fcc phase, but the two sets of reflections belong to the bcc and $D0_3$ phases, we assume that the darker majority phase is bcc, while the lighter minority phase is $D0_3$ that is further enriched in the two heaviest elements Ga and Ni with respect to the bcc phase. The domains of the $D0_3$ phase are likely present already in the $x = 1.3$ alloy, where careful inspection of its BSE image on a zoomed scale (Fig. 3e) reveals that the matrix is not of a uniform grey color, but contains some slightly brighter regions (one is enclosed by a dashed circle), which can be associated with the $D0_3$ precipitates within the bcc phase, but the $D0_3$ fraction is not yet observed in the XRD pattern because its specific reflections are still below the sensitivity limit. The position of the encircled $D0_3$ precipitate on a larger-scale BSE image of the $x = 1.3$ alloy (Fig. 3d) is indicated by a white arrow.

3.3. Chemical composition determination by SEM-EDS

Chemical compositions of the individual phases in the alloys on the SEM-EDS spatial scale (where the characteristic X-ray signals are coming from the interaction volume of a few μm cross-dimension) were determined by EDS point analysis and elemental mapping. The so determined compositions are denoted in the following as the SEM-EDS compositions. The signals for the point analysis were averaged from ten points, separated by a minimum distance of 20 μm. For each chemical element, the scatter of the concentration values over the ten points was very small, so that the average SEM-EDS compositions of each phase, reported in the Table 2 are accurate to within ±1 at.%. For the $x = 0.4$ alloy, the dendrites' core composition (in at.%, rounded to first integers) is $Ga_9Ni_{10}Co_{27}Cr_{27}Fe_{27}$, the dendrites' boundary composition is $Ga_{17}Ni_{17}Co_{23}Cr_{23}Fe_{20}$, while the composition of the minor interdendritic region is $Ga_{17}Ni_{11}Co_{32}Cr_{20}Fe_{20}$. As expected from the SEM-BSE image of Fig. 3a, the dendrites' boundaries are enriched quite significantly in the Ga and Ni elements and consequently depleted in the Co, Cr and Fe, as compared to the dendrites' cores, while the interdendritic regions are enriched in Cr. Upon increasing the $(GaNi)_x$ content, the bcc phase appears and its composition changes monotonously from $Ga_{24}Ni_{20}Co_{19}Cr_{19}Fe_{18}$ (for $x = 0.7$) to $Ga_{25}Ni_{24}Co_{17}Cr_{17}Fe_{17}$ (for $x = 1.6$), while the fcc phase composition changes from $Ga_9Ni_{10}Co_{27}Cr_{27}Fe_{27}$ (for $x = 0.4$) to $Ga_{17}Ni_{19}Co_{21}Cr_{21}Fe_{22}$ (for $x = 1.3$). The composition of the $D0_3$ phase in the $x = 1.6$ alloy is $Ga_{27}Ni_{28}Co_{15}Cr_{15}Fe_{15}$, being additionally enriched in the Ga and Ni (and consequently depleted in the Co, Cr and Fe) with respect to the bcc phase ($Ga_{25}Ni_{24}Co_{17}Cr_{17}Fe_{17}$) in that alloy. The SEM-EDS elemental maps of the $x = 0.7$ alloy that is representative of all five alloys are shown in Fig. 4 (the elemental maps of other alloys are shown in Figs. S1–S4 of the Supplementary material). An enrichment of the bcc phase in the Ga and

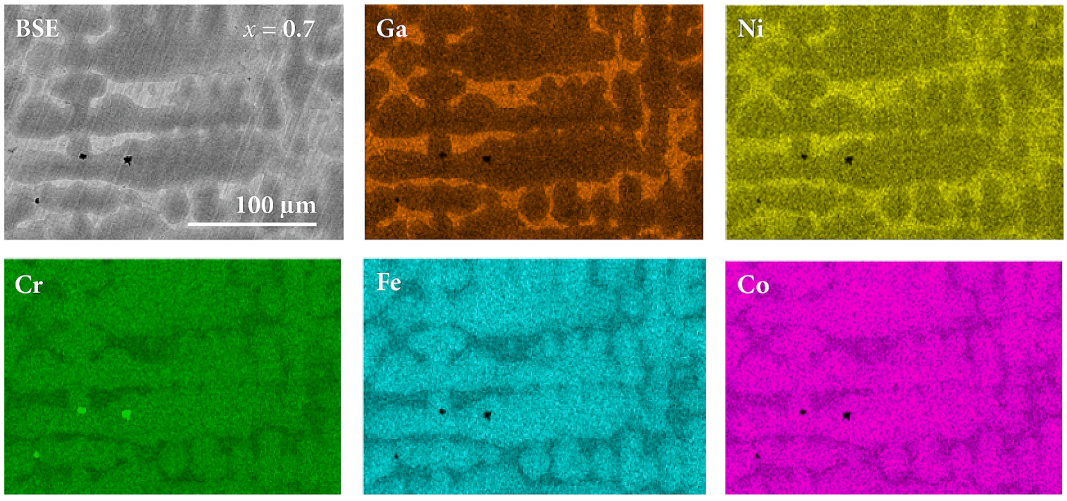

Fig. 4. SEM-BSE image (upper left panel) and SEM-EDS elemental maps of the $x = 0.7$ alloy.

Ni and its depletion in the Co, Cr and Fe is evident, while the opposite holds for the fcc phase. Some unreacted small pure-Cr grains are also present, as observed in the Cr map. Otherwise, the distribution of all five elements on the 100-µm scale appears homogeneous.

3.4. Nanostructure of the alloys by STEM

The methods of BF-STEM and HAADF-STEM imaging and STEM-EDS point- and line composition analysis and elemental mapping were used

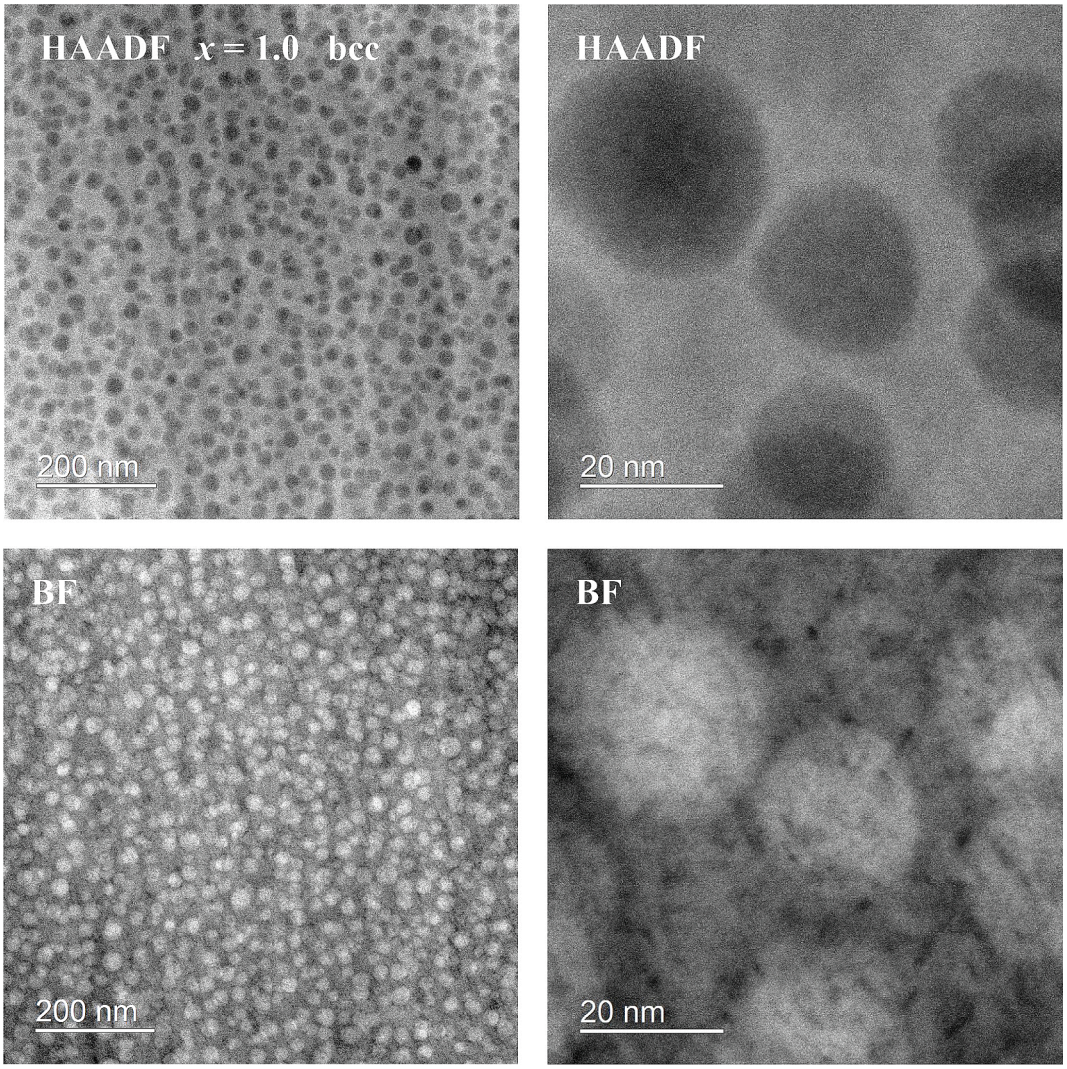

Fig. 5. HAADF-STEM and BF-STEM images of the bcc phase in the $x = 1.0$ alloy on two magnification scales.

to determine the nanostructure and local chemical composition of the bcc and fcc phases in the $(GaNi)_xCoCrFe$ alloys. For the STEM investigations, two lamellae of about 50 nm thickness were cut by the FIB technique using gallium atoms, one in the fcc phase of the $x = 0.4$ alloy and the other in the bcc phase of the x $= 1.0$ alloy.

We present first the results on the nanostructure of the $x = 1.0$ bcc phase. In Fig. 5, the HAADF-STEM and BF-STEM images are shown on two magnification scales. A pronounced nanostructure is observed, where a large amount of spherical-like domains of one chemical composition (conveniently denoted as the "nanoparticles") of cross dimensions in the range 10–30 nm are embedded in a matrix of a different composition. The STEM-EDS elemental maps are shown in Fig. 6, revealing that the nanoparticles are highly enriched in Cr and contain also some Fe and Co, while the matrix is basically Cr-free, but contains all other four elements. The STEM-EDS point analysis has yielded the composition of the matrix $Ga_{43}Ni_{22}Co_{18}Cr_3Fe_{14}$. The measured Cr concentration of 3 at.% is so small that the Cr signal was very likely collected from the environment (the electron beam has "touched" a nanoparticle upon traveling through the matrix). By neglecting the presence of Cr, the composition of the Cr-free matrix is then $Ga_{44}Ni_{23}Co_{19}Fe_{14}$, hence being abundant in the nonmagnetic Ga, and containing the three FM elements Co, Fe and Ni. The STEM-EDS composition of the nanoparticle was determined as $Ga_8Ni_5Co_{11}Cr_{64}Fe_{12}$. By inspecting the STEM-EDS elemental maps of Fig. 6, it is apparent that there is in fact very little (or no) Ga and Ni present in the nanoparticles and the signals of these two elements are likely collected from the environment. This is a reasonable assumption, because the cross dimension of the investigated nanoparticle was 30 nm, while the lamella thickness was 50 nm, so that some signal from the matrix was inevitably collected. By neglecting the presence of Ga and Ni, the nanoparticle composition is about $Co_{13}Cr_{73}Fe_{14}$, being highly enriched in Cr and containing a mixture of the two FM elements Co and Fe and one AFM element Cr. The above analysis is supported by the STEM-EDS elemental line profiles over the path of 80-nm length that crosses one nanoparticle (Fig. 7). A negligible amount of Ni in the nanoparticle and a negligible amount of Cr in the matrix are clearly evident, while the concentrations of other elements, both in the matrix and in the nanoparticle are in fair agreement with the values determined by STEM-EDS point analysis. The main discrepancy is the Ga concentration in the nanoparticle (about 10 at.%), which may be real, so that the nanoparticles may also contain some nonmagnetic Ga (but its origin from the environment cannot be excluded).

Next we present the results on the nanostructure of the $x = 0.4$ fcc phase. The HAADF-STEM and BF-STEM images on the 100-nm scale are presented in Fig. 8. Contrary to the bcc phase, no nanodecomposition into chemically different domains could be observed, so that the fcc phase is not nanostructured, but homogeneous also on this scale. The remaining contrasts in the HAADF and BF images (a bit corrugated surface, some black dots and short stripes in the BF image) are mainly dislocations, introduced either during the material synthesis or by mechanical forces during the FIB treatment. The STEM-EDS elemental maps are shown in Fig. 9, confirming homogeneous distribution of all five elements in the fcc phase on the nanometric scale and consequently the absence of nanostructure. The STEM-EDS point analysis has given the local chemical composition $Ga_{12}Ni_9Co_{28}Cr_{23}Fe_{28}$, which is in fair agreement with the SEM-EDS (average) composition of the fcc phase in the interior of the dendrites $Ga_9Ni_{10}Co_{27}Cr_{27}Fe_{27}$. The STEM-EDS elemental line profiles over the path of 250-nm length (Fig. 10) confirm homogeneous distribution of the elements and the absence of nanostructure in the fcc phase on the nanometric scale.

3.5. Magnetic properties

The $(GaNi)_xCoCrFe$ HEAs were characterized magnetically by the magnetization versus the magnetic field, $M(H)$, curves and by the temperature-dependent magnetization, $M(T)$. The $M(H)$ curves of all five alloys at $T = 300$ K for the magnetic field sweep $\mu_0 H = \pm 7$ T are presented in Fig. 11a. All curves exhibit a rectangular-like $M(H)$ characteristic with an abrupt step at $H = 0$ and quick saturation to a plateau. Such dependence is typical of soft ferromagnets. The saturated magnetization M_s increases systematically with the increasing $(GaNi)_x$ content. The saturation magnetic polarization $J_s = \mu_0 M_s$ of the alloys (taken at the field value of 7 T), as a function of x is shown in the inset (i) of Fig. 11a. The J_s values of the $x = 1.6$ and 1.3 alloys that amount to 0.55 and 0.50 T, respectively, are reasonably high for a technologically

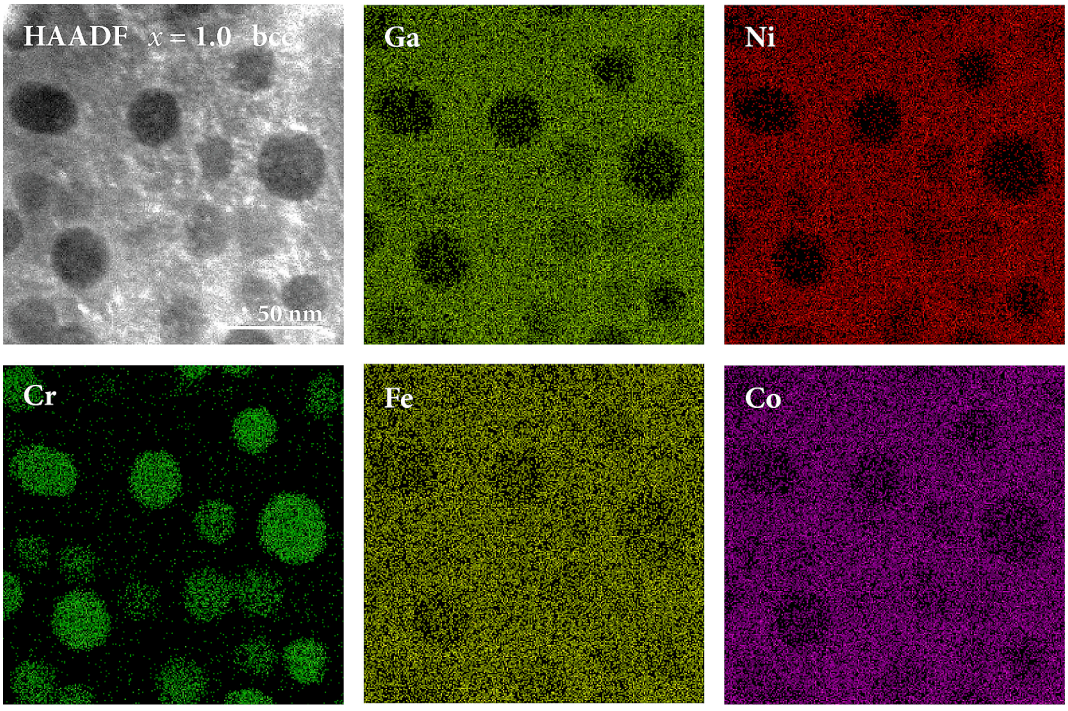

Fig. 6. HAADF-STEM image (upper left panel) and STEM-EDS elemental maps of the bcc phase in the $x = 1.0$ alloy.

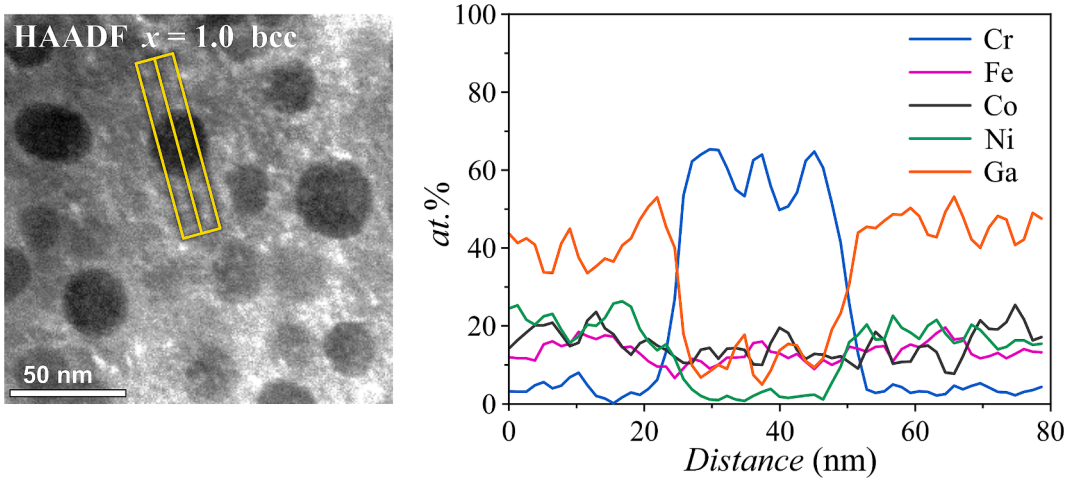

Fig. 7. STEM-EDS compositional line profiles of the elements in the bcc phase of the $x = 1.0$ alloy, measured along an 80-nm path that crosses one nanoparticle. The path is drawn in the HAADF image (left panel).

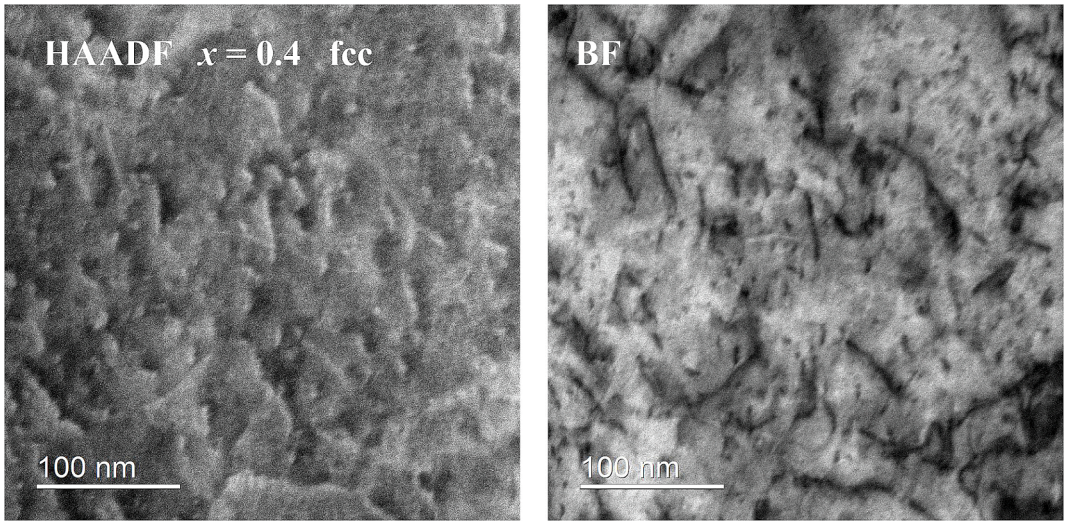

Fig. 8. HAADF-STEM and BF-STEM images of the fcc phase (the matrix) in the $x = 0.4$ alloy.

interesting magnetically soft material [14,15]. For the $x = 0.4$ alloy, a tiny step in the $M(H)$ can still be observed at $H = 0$, but the ferromagnetic component of the signal is very small. Away from the step at $H = 0$, the $M(H)$ relation is linear paramagnetic (the $M(H)$ curve is shown on an expanded vertical scale in the inset (*ii*) of Fig. 11a), so that this alloy behaves predominantly paramagnetically.

The hysteresis loops at 300 K of the samples $x \geq 0.7$ are shown on an expanded scale in Fig. 11b. Palladium correction was applied to subtract the remanent field of the superconducting magnet of the employed SQUID magnetometer. The coercivity as a function of the $(GaNi)_x$ content is shown in the inset of Fig. 11b. All alloys show the coercive field of about $\mu_0 H_c \approx 0.5$ mT (or $H_c \approx 400$ A m^{-1}). The commonly accepted limit to classify ferromagnets as magnetically soft is $H_c < 1000$ A m^{-1} [15], and the alloys conform to this criterion. The shape of the hysteresis curves is also typical FM and the curves close up in a quite small field of about 3 mT.

The FM Curie temperatures of the alloys were determined by performing measurements of the temperature-dependent magnetization in the interval from RT to 1000 K using a furnace. A magnetic field of 10 mT was applied and the measurements were performed upon heating. Since the HEA state is in principle a metastable state that is likely to change upon thermal annealing of the material at high temperatures, we have repeated the $M(T)$ measurement for each alloy several times (up to four times), in order to see whether some change of the magnetization (that is sensitive to even minute structural/chemical changes) has happened during the exposure of the material to high temperatures. The measurements have revealed that the $M(T)$ curve of the 1st (virgin) run was always slightly different from the subsequent (non-virgin) runs, for which the differences were smaller. This is demonstrated in Fig. 12a, where the $M(T)$ curves of the $x = 1.3$ alloy of four consequent heating runs are presented. The differences are not large, confirming that the material is quite stable upon thermal cycling up to 1000 K. In Fig. 12b, the $M(T)$ curves of all alloys, obtained in the 2nd run are presented on the same graph. A clear FM behavior is observed for the $x = 0.7$, 1.0, 1.3 and 1.6 alloys, with the Curie temperatures of $T_C \approx 750$, 725, 715 and 700 K, respectively. The Curie temperatures hence decrease slightly with the increasing $(GaNi)_x$ content (because the concentration of nonmagnetic Ga is increased). For the $x = 0.4$ alloy, the FM component in the $M(T)$ signal was so small that the Curie temperature could not be determined. The $M(T)$ results also confirm that the inclusion of the low-melting-point element Ga into the alloys did not reduce their melting points significantly.

The temperature dependence of the $M(H)$ curves, the saturation magnetic polarization J_s and the coercive field H_c were investigated in

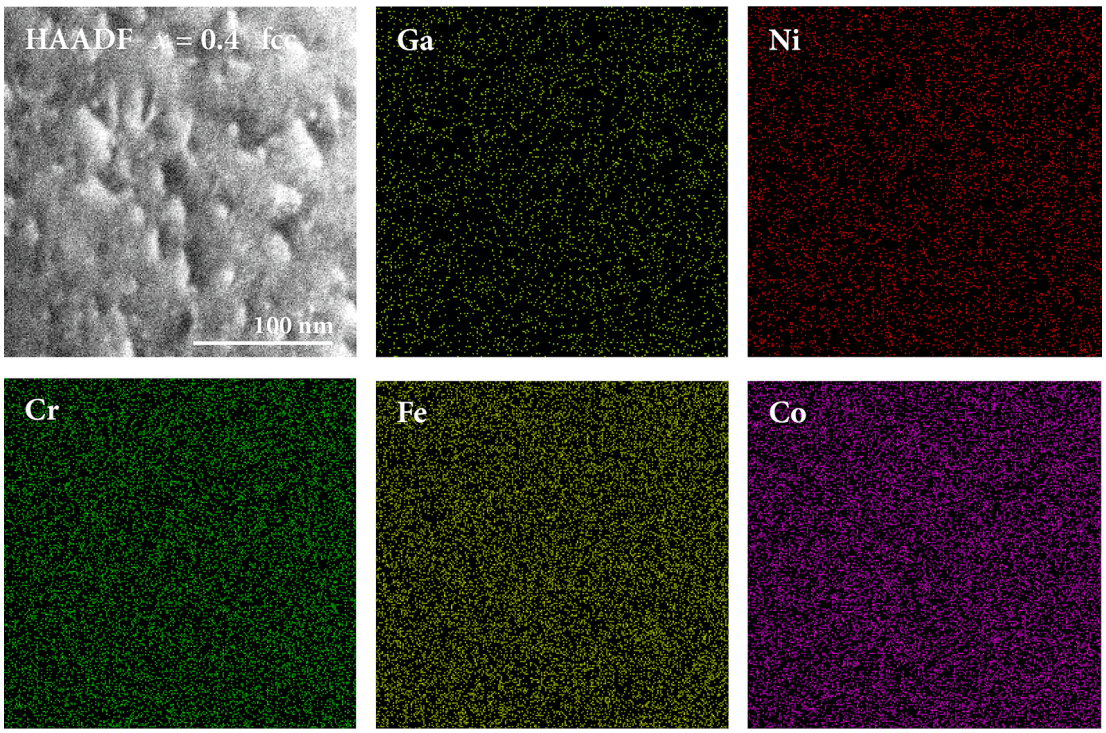

Fig. 9. HAADF-STEM image (upper left panel) and STEM-EDS elemental maps of the fcc phase (the dendrites' interior) in the $x = 0.4$ alloy.

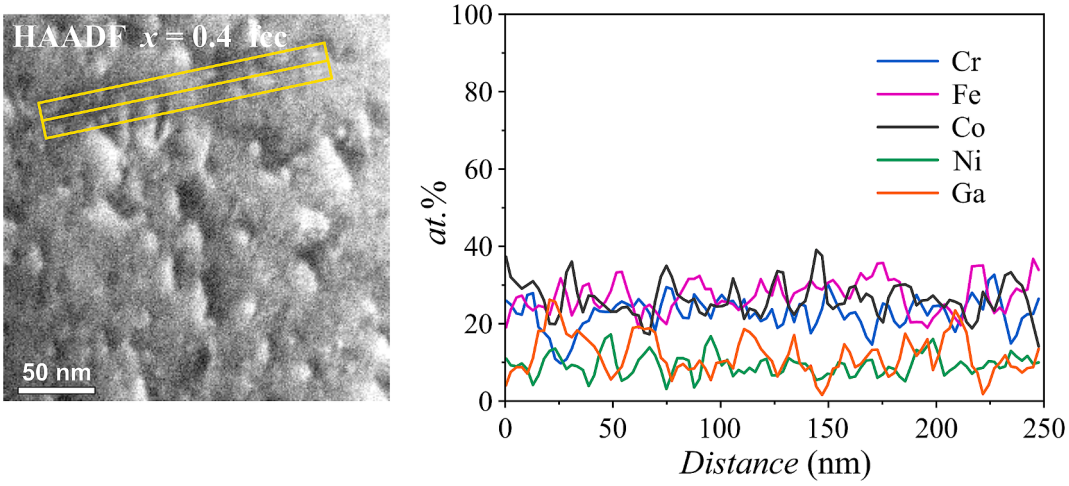

Fig. 10. STEM-EDS compositional line profiles of the elements in the fcc phase (the dendrites' interior) of the $x = 0.4$ alloy, measured along a 250-nm path. The path is drawn in the HAADF image (left panel).

the temperature interval between 400 and 5 K. Below we present the results for the strongest-magnetic alloy $x = 1.6$, which are representative (qualitatively) of all FM alloys. The $M(H)$ curves at five temperatures in that interval are displayed in Fig. 13a, showing that the rectangular shape typical of soft ferromagnets is preserved at all temperatures, with a slight increase of the saturated magnetization M_s plateau upon cooling. The $J_s(T)$ relation is shown in the inset of Fig. 13a, where it is seen that the saturation magnetic polarization increases from 0.47 T at 400 K to 0.64 T at 5 K. The temperature-dependent hysteresis curves widen upon cooling (Fig. 13b). The coercive field $H_c(T)$ relation is shown in the inset, where an increase of H_c from 200 A m^{-1} at 400 K to 1160 A m^{-1} at 5 K is evident. Magnetic softness of the material can thus be claimed in the entire investigated temperature range.

3.6. Magnetostriction

Magnetostrictive properties of the $(GaNi)_xCoCrFe$ alloys were investigated by measuring the linear magnetostriction (the magnetostrictive strain) $\lambda = \Delta l/l$, defined as the fractional change in length of the material in the direction of magnetization during the magnetizing process. The magnetostriction of isotropic polycrystalline materials, like the investigated cubic HEAs, is fully characterized by a single parameter λ (in dimensionless units μm m^{-1} or 10^{-6}), which can be either positive or negative. In a large enough magnetic field, the magnetostrictive strain saturates to a value λ_s, which is then used to compare different magnetostrictive materials.

The magnetostriction experiments were performed at RT in a magnetic field sweep $\mu_0 H = \pm 0.2$ T by using a strain gage sensor [16]. A pure aluminum metal sample that possesses zero magnetostriction was

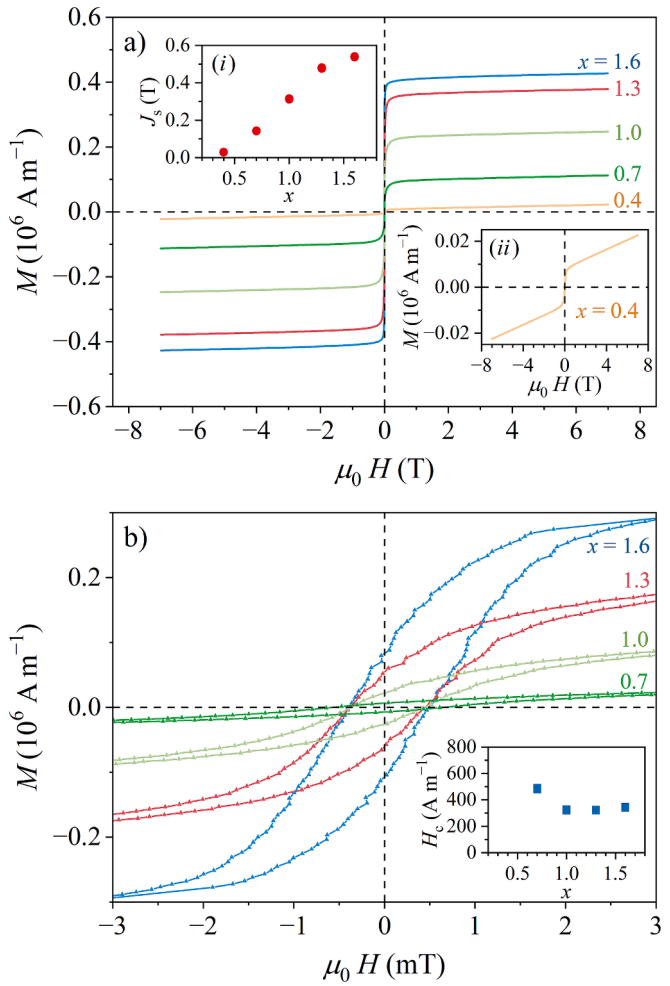

Fig. 11. (a) The $M(H)$ curves of the $(GaNi)_xCoCrFe$ alloys at $T = 300$ K for the magnetic field sweep $\mu_0 H = \pm 7$ T. The inset (*i*) shows the saturation magnetic polarization J_s as a function of x , while the inset (*ii*) shows the $M(H)$ curve of the $x = 0.4$ alloy on an expanded vertical scale. (b) Hysteresis loops of the alloys $x \geq 0.7$ on an expanded scale. The inset shows the coercive field H_c as a function of x.

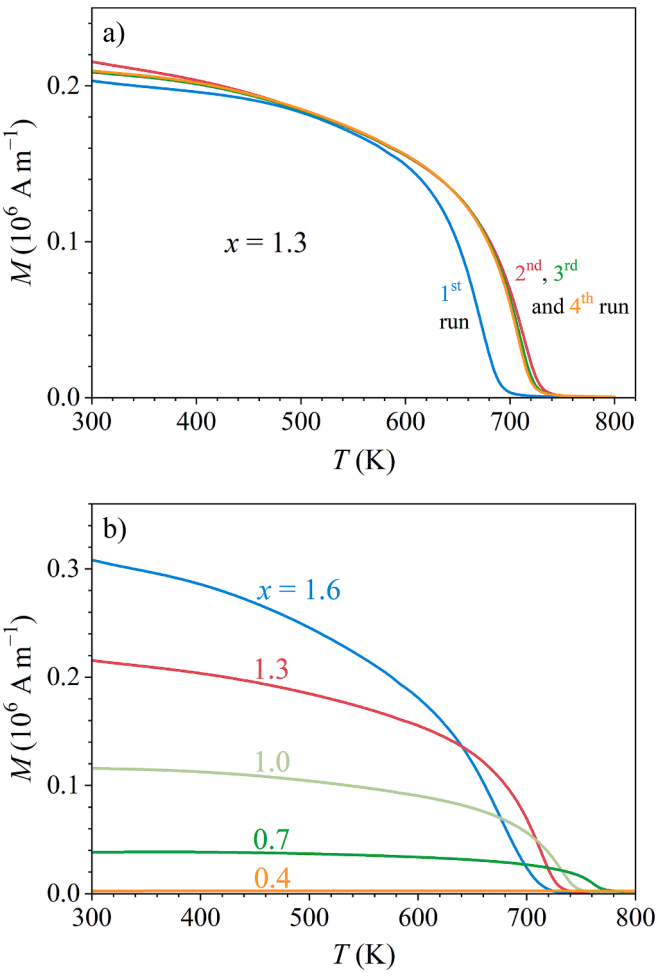

Fig. 12. (a) Magnetization versus temperature, $M(T)$, curves of the $x = 1.3$ alloy measured in a magnetic field $\mu_0 H = 10$ mT in four consequent heating runs within the temperature interval 300–1000 K (the data below 800 K are shown only). (b) $M(T)$ curves of all alloys, obtained in the 2nd run.

used to check whether the experimental setup itself contains some "background" signal, but no magnetostriction could be detected. The magnetostrictive strain curves $\lambda(H)$ of all five investigated alloys are shown in Fig. 14a. The $\lambda(H)$ curve of the $x = 0.4$ sample is practically zero, which is in agreement with the magnetization measurements that indicate its marginally ferromagnetic character at RT, while the $\lambda(H)$ curves of the other alloys are negative and the saturation value λ_s increases slightly (in the absolute sense) with the increasing $(GaNi)_x$ content. The sample $x = 1.6$ shows the largest negative value $\lambda_s = -3$ μm m^{-1}. The saturation magnetostriction coefficient λ_s, as a function of the $(GaNi)_x$ content is shown in Fig. 14b. The close-to-zero λ_s values in the range between 0 and −3 μm m^{-1} classify the $(GaNi)_xCoCrFe$ HEAs as vanishing-magnetostriction materials. For comparison, the RT λ_s values of pure Ni and Co (FM) metals amount to −35 and −60 μm m^{-1}, respectively, Metglass 2826 (a-$Fe_{40}Ni_{40}P_{14}B_6$) possesses the value $\lambda_s =$ 11 μm m^{-1}, while some mixed rare-earth–iron alloys exhibit λ_s values up to 2000 μm m^{-1} [17].

3.7. Electrical resistivity

Electrical resistivity is another technologically relevant physical parameter for the characterization of magnetically soft materials. High resistivity is desired in order to minimize energetic losses due to eddy currents in AC applications. The electrical resistivity ρ of the $(GaNi)_x$-CoCrFe alloys was determined in the temperature interval 2–400 K and the results are shown in Fig. 15. The absolute resistivity values are precise to within ±10 %, due to errors in the samples' dimensions determination (length and cross section), inhomogeneity of the electrical contacts and grain boundaries in a polygrain material. For that reason, no systematic variation of the resistivity with the $(GaNi)_x$ content could be identified. The resistivities are typical metallic, with a positive temperature coefficient and linear variation above about 25 K. The 300-K resistivity values are in the range $\rho_{300K} = 110$–130 μΩ cm, while the 2-K values are in the range $\rho_{2K} = 95$–120 μΩ cm. These values are high enough for a good magnetically soft material. For comparison, the resistivity of the widely used commercial soft magnetic material non-oriented electrical steel (silicon steel $Fe_{97}Si_3$, type M270-35A) amounts to $\rho_{300K} = 40$ μΩ cm and $\rho_{2K} = 30$ μΩ cm [3], while the resistivities of the magnetically soft and vanishing-magnetostriction HEAs $AlCoFeNiCu_x$ ($x = 0.6$–3.0) are in the range $\rho_{300K} = 45$–75 μΩ cm and $\rho_{2K} = 35$–65 μΩ cm [5].

4. Discussion

The experiments show convincingly that the bcc phase is ferromagnetic, while the fcc phase is paramagnetic (at least at RT and above). This is further supported by the graph presented in Fig. 16, where the saturation magnetization M_s of the alloys at $T = 300$ K is plotted versus

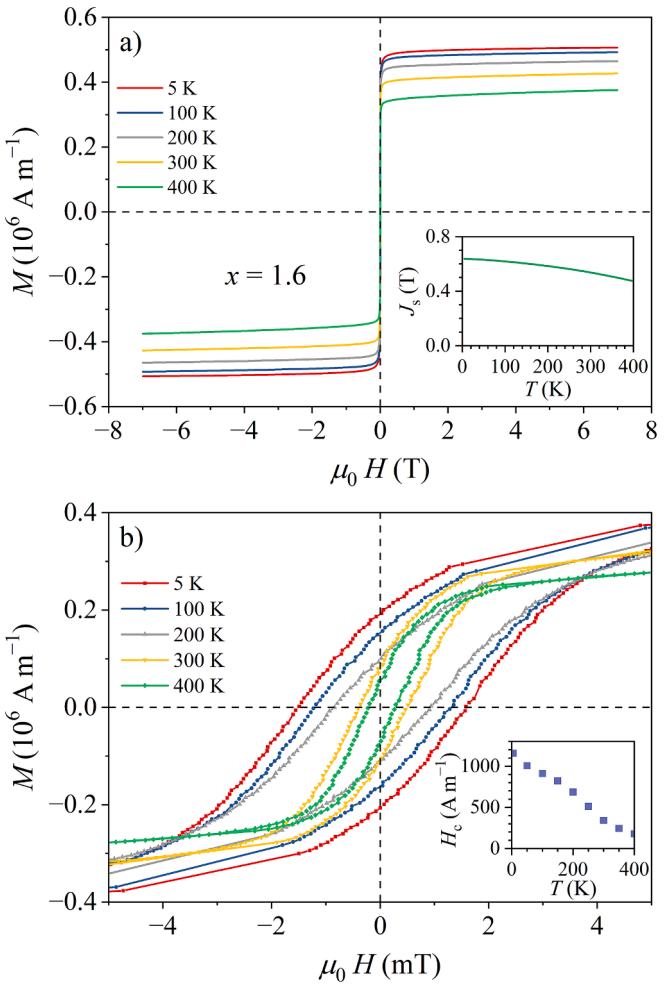

Fig. 13. (a) Temperature-dependent $M(H)$ curves of the $x = 1.6$ alloy in the interval between 400 and 5 K. The inset shows the temperature-dependent saturation magnetic polarization J_s. (b) Temperature-dependent hysteresis curves of the $x = 1.6$ alloy on an expanded scale. The inset shows the temperature-dependent coercive field H_c.

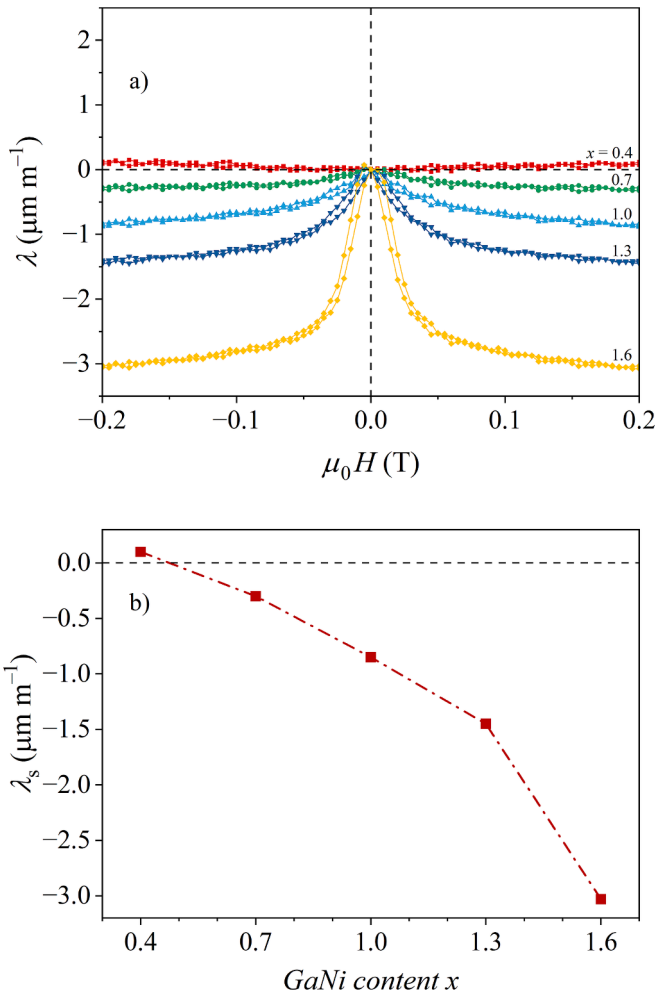

Fig. 14. (a) Magnetostrictive strain curves $\lambda(H)$ of the $(GaNi)_xCoCrFe$ alloys at $T = 300$ K for the magnetic field sweep $\mu_0 H = \pm 0.2$ T. Small up-down hysteresis in the vicinity of $H = 0$ can be observed for the alloys with $x \geq 1.0$. (b) Saturation magnetostriction coefficient λ_s as a function of the $(GaNi)_x$ content.

the bcc phase fraction as determined by XRD (for the $x = 1.6$ alloy, M_s is plotted both versus the bcc fraction only and versus the sum of the bcc + $D0_3$ fractions). For the alloys $x = 0.7$ to 1.3, a clear one-to-one linear relation is evident, where the solid line is the least-squares fit through these points. The point of the $x = 0.4$ alloy also falls on this line, but the origin of the tiny FM signal in this alloy is not obvious, because XRD confirms only the presence of the fcc phase. It is likely that precipitates of the bcc phase in trace quantities are already present in this alloy, but are still below the sensitivity threshold of the powder XRD technique (about 1 wt%). The two points belonging to the $x = 1.6$ alloy do not fall on this line. The fit passes between these two points, being closer to the point corresponding to the sum of the bcc + $D0_3$ fractions (amounting to 100 wt%) than to the point corresponding to the bcc fraction only, indicating that the $D0_3$ phase is also ferromagnetic. In the following, we shall not consider the magnetism of the $D0_3$ phase separately, but will treat it in the context of the bcc phase. The experimental fact that the bcc phase is ferromagnetic, while the fcc phase is paramagnetic, is not trivial to understand. The SEM-EDS (average) compositions of the bcc and fcc phases given in Table 2 are not so much different to yield an obvious reason for the ferromagnetic character of the former and the paramagnetic character of the latter. The clue is the nanostructure of the two phases, where the bcc phase is highly nanostructured, while the fcc is not.

The ferromagnetism of the bcc phase can be qualitatively understood

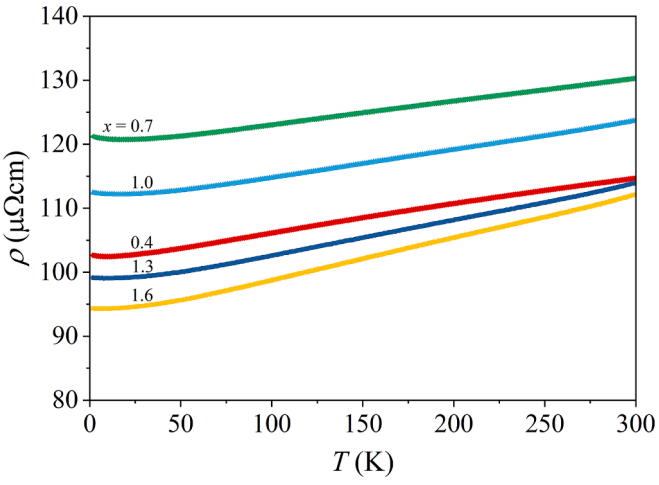

Fig. 15. Electrical resistivity ρ of the $(GaNi)_xCoCrFe$ alloys in the temperature interval 2–400 K.

by considering that the nanostructure is composed of the Ga-Co-Fe-Ni matrix (its STEM-EDS chemical composition in the $x = 1.0$ alloy is about $Ga_{44}Ni_{23}Co_{19}Fe_{14}$) that contains three FM elements Co, Fe and Ni,

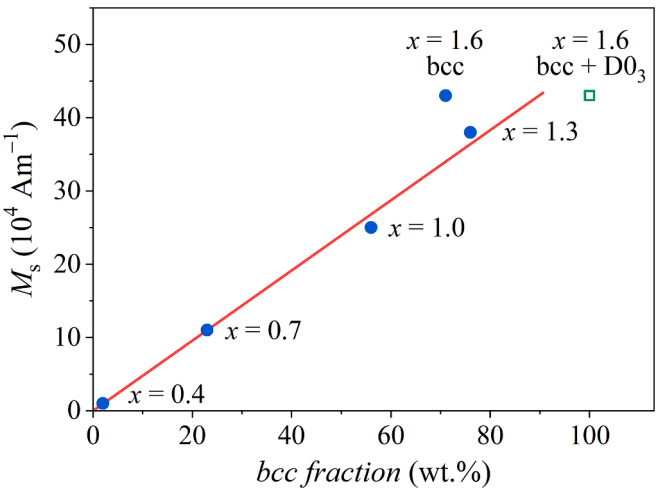

Fig. 16. Saturation magnetization M_s of the alloys at $T = 300$ K versus the bcc phase fraction (for the $x = 1.6$ alloy, M_s is plotted both versus the bcc fraction only and versus the sum of the bcc + $D0_3$ fractions). Solid line is the least-squares fit through the points of the $x = 0.7$ to 1.3 alloys.

but no AFM Cr, while the nanoparticles embedded in the matrix are basically Co-Cr-Fe, being a mixture of two FM elements Co and Fe and one AFM element Cr. In a metallic environment, the spins of the magnetic elements distributed on a chemically disordered lattice are coupled by the indirect exchange interaction via the conduction electrons and the magnetic state is exchange dominated, because the random local magnetic anisotropy in 3*d* magnetic alloys is generally too weak to pin the magnetization direction at the atomic scale [18]. *Ab initio* calculations for the Cantor alloy CoCrFeMnNi have predicted that the pairs of like and unlike FM neighbors (Co-Co, Fe-Fe, Ni-Ni, Co-Fe, Co-Ni and Fe-Ni) all show preference for a parallel (FM) spin alignment, while the spins of the Cr-Cr pairs and the unlike pairs of Cr with the Co, Fe and Ni align antiparallel (AFM) [19–23]. Adopting these theoretical results, it is straightforward to consider that in the bcc matrix of composition Ga-Co-Fe-Ni, there exist only the FM type indirect exchange interactions and the matrix is hence ferromagnetic. The CoCrFe-rich nanoparticles behave differently. Their composition is highly enriched in the AFM element Cr (it is about $Co_{13}Cr_{73}Fe_{14}$), so that the majority of the elemental pairs (Cr-Cr, Co-Cr, Fe-Cr) align their spins antiparallel and the nanoparticles are consequently spin-compensated, being either weakly magnetic or nonmagnetic, as compared to the matrix. It is also known that in the Co-Cr-Fe bulk ferromagnets, there exists a miscibility gap below a certain temperature, which clusters the AFM Cr atoms together and the FM Co and Fe atoms together into spatially segregated regions [24–27]. For the above Co-Cr-Fe nanoparticles (that are highly enriched in Cr), the miscibility gap could yield an AFM-ordered Cr majority region (perhaps the core of the nanoparticle) with weak (or no) magnetic signal and the FM-ordered minority CoFe region (perhaps the nanoparticle's shell) with the FM signal that would add to the FM signal of the matrix. However, it is a question whether a miscibility gap could indeed occur in the nanoparticles of so small dimensions (10–30 nm), because nanodimensional objects behave magnetically differently from the bulk. The STEM-EDS elemental maps and elemental line profiles presented in Figs. 6 and 7 do not give any hint of the elemental segregation and hence the miscibility gap in the nanoparticles. Here we mention that similar Co-Cr-Fe nanoparticles with a core–shell structure (where the core is highly enriched in Cr, while the shell of 2 nm thickness is CoFe-rich) were indeed observed in the related $Al_{28}Co_{20}Cr_{11}Fe_{15}Ni_{26}$ HEA [28,29], but those nanoparticles were significantly larger, of the average diameter 64 nm, so that a direct comparison with the smaller nanoparticles in the $(GaNi)_xCoCrFe$ HEAs is questionable.

The paramagnetic character of the fcc phase can be considered along the same steps, by taking into account the experimental fact that this phase is not nanostructured, but appears as a chemically homogeneous mixture of five elements on both the nm- and the μm scales (the local STEM-EDS composition of the fcc phase (the dendrites' interior) in the $x = 0.4$ alloy $Ga_{12}Ni_9Co_{28}Cr_{23}Fe_{28}$ is in fair agreement with its SEM-EDS average composition $Ga_9Ni_{10}Co_{27}Cr_{27}Fe_{27}$). The Cr-Cr like pairs and the unlike pairs of Cr with the Co, Fe and Ni favor antiparallel spin alignment, while the spins of the like and unlike pairs of the Co, Fe and Ni atoms tend to align parallel, so that there is a competition between the FM and AFM couplings, which causes magnetic frustration of the spin system. Such disordered spin systems usually form a collective magnetically frustrated state known as a spin glass [30]. The spin glass state is a low-temperature phenomenon, occurring typically at temperatures of the order of 10 K above absolute zero, while at higher temperatures such a state is paramagnetic. The hypothesis that the fcc phase in the $(GaNi)_xCoCrFe$ alloys is paramagnetic at elevated temperatures, but undergoes a spin glass transition at low temperatures was tested on the $x = 0.4$ fcc alloy. The linear paramagnetic $M(H)$ relation with a positive slope at 300 K of this alloy shown in the inset (*ii*) in Fig. 11a confirms that it is paramagnetic at RT (here we neglect the tiny FM component that very likely originates from the trace amounts of the bcc phase). Spin glasses undergo a kinetic spin-freezing transition from the high-temperature paramagnetic phase to the low-temperature spin glass phase at the spin-freezing temperature T_f, which delimits the high-temperature ergodic (thermodynamic equilibrium) region of the spin system from the low-temperature nonergodic (out-of-equilibrium) region. Below T_f (in the spin glass phase), the experimentally measurable physical parameters become frequency-dependent, depending on the frequency observation window of a given experimental technique [30]. Broken ergodicity of the spin system in the spin glass phase is a consequence of the fact that spin fluctuation times become macroscopically long, so that the system can no longer reach thermal equilibrium on the accessible experimental frequency scale. A convenient physical quantity to prove the spin glass transition is the AC magnetic susceptibility, which shows a broad cusp at the spin-freezing temperature and the position of the cusp on the temperature axis is frequency-dependent, shifting to higher temperatures at higher frequencies. The AC susceptibility of the $x = 0.4$ alloy was measured between 300 and 1.8 K in a sinusoidal magnetic field of amplitude $\mu_0 H_0 = 0.2$ mT at logarithmically spaced frequencies between 1 and 1000 Hz. A frequency-dependent cusp was indeed observed in the real part of the AC susceptibility χ', which is presented on an expanded temperature interval around the cusp in Fig. 17. At the lowest frequency $\nu = 1$ Hz, the maximum in χ' occurs at 6.4 K and then shifts monotonously to 6.7 K for $\nu = 1000$ Hz. This behavior is a clear indication of the spin-freezing transition to a nonergodic state. The temperature of the maximum in χ' is conveniently defined as the frequency-dependent spin-freezing temperature $T_f(\nu)$. The $T_f(\nu)/T_f(1\text{Hz})$ relation is shown in the inset of Fig. 17. A convenient parameter to characterize spin glasses is the fractional shift of $T_f(\nu)$ per decade of frequency, $\Gamma = \Delta T_f / T_f \Delta(\log\nu)$, where the data from the inset in Fig. 17 yield $\Gamma = 1.4 \times 10^{-2}$. This value falls into the range typical of spin glasses, where the values $\Gamma \approx 10^{-2}$–10^{-3} are common, while for superparamagnets below the blocking temperature, the Γ values are one or two orders of magnitude larger [31]. The AC susceptibility hence confirms the spin glass state of the fcc phase below the spin freezing temperature $T_f \approx 6.4$ K, while at $T > T_f$, the fcc phase is paramagnetic.

The ferromagnetism of the $(GaNi)_xCoCrFe$ HEAs hence originates from the Ga-Co-Fe-Ni matrix of the nanostructured bcc phase. The magnetic softness of the matrix follows from the chemically disordered statistical distribution of the magnetic Co, Fe and Ni and the nonmagnetic Ga on the bcc lattice, where the CoFeNi-enriched FM domains of a nanometric size are more or less randomly intermixed with Ga-enriched (less magnetic or nonmagnetic) domains of a similar size. In such structures, magnetic softness is a nanomagnetic effect, because the CoFeNi-enriched FM domains of that smallness are magnetically single-

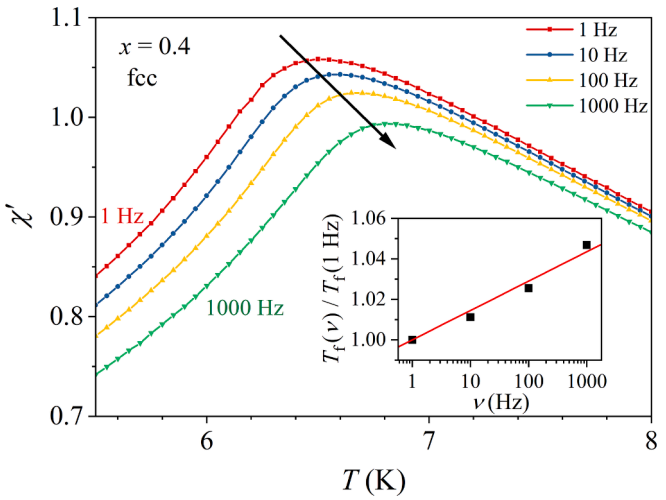

Fig. 17. Frequency-dependent cusp in the real part of the AC susceptibility χ' of the $x = 0.4$ fcc alloy on an expanded temperature scale between 5.5 and 8 K for logarithmically spaced frequencies of the AC magnetic field between 1 and 1000 Hz. The frequency-dependent spin freezing temperature $T_f(\nu)$ is defined as the temperature of the $\chi'(\nu)$ maximum. The skew arrow indicates the shift of the maximum to higher temperatures with the increasing frequency. The $T_f(\nu)/T_f(1\text{Hz})$ relation is shown in the inset. Note that χ' is dimensionless, because it is derived from the volume magnetization.

domain "particles", and since the particles with randomly oriented FM axes are exchange-coupled across the boundaries, exchange averaging of the magnetic anisotropy to zero takes place, as known from the literature [4]. The same effect is responsible for the almost perfect magnetic softness of the related HEAs CoFeNiPdCu [3] and $AlCoFeNiCu_x$ [5]. It is straightforward to consider that the exchange averaging of magnetic anisotropy is the general principle underlying the magnetic softness also of other CoFeNi-containing HEAs (numerous in number) reported in literature [20,32–41].

The above-described nanostructure of the FM bcc matrix additionally results in its vanishing magnetostriction. The nanometer-size CoFeNi-enriched FM domains are so small that the magnetostrictive strain in an external magnetic field cannot change their shape and size considerably. Moreover, even if the magnetostrictive strain would still be effective at such small scales, random orientation of the domains' ferromagnetic axes would cause their elongation/contraction in random spatial directions, which would average the net magnetostrictive strain of the material to zero and result in vanishing magnetostriction. The magnetic softness and vanishing magnetostriction thus go hand in hand in this type of 3*d* FM HEAs.

5. Conclusions

The $(GaNi)_xCoCrFe$ HEAs possess the functional combination of magnetic softness and vanishing magnetostriction, classifying them as supersilent materials for the audio-frequency AC electromagnetic applications. The magnetic-softness and magnetostriction parameters of the $x = 1.6$ alloy (saturation magnetic polarization $J_s = 0.55$ T, coercive field $H_c \approx 400$ A m^{-1}, Curie temperature $T_C = 700$ K, saturation magnetostriction coefficient $\lambda_s = -3$ μm m^{-1} and high RT electrical resistivity $\rho_{300K} \approx 110$ μΩ cm) are about the same as those of the $AlCoFeNiCu_{2.0}$ alloy, the first reported supersilent HEA [5]. The parameters of the $x = 1.3$ alloy are only insignificantly different, so that the $(GaNi)_{1.3}CoCrFe$ and $(GaNi)_{1.6}CoCrFe$ HEAs both possess application-relevant supersilent characteristics. Possessing very small coercive field (small width of the $M(H)$ hysteresis curve) and high electrical resistivity that both determine the electromagnetic losses in AC applications, the materials are also energy-efficient.

Regarding the combination of magnetic softness and vanishing magnetostriction, the $(GaNi)_xCoCrFe$ HEAs perform comparably to the $AlCoFeNiCu_x$ HEAs, but better than other reported multi-component alloys, either four-component or five-component. The five-component HEAs $Fe_xCo_{1-x}NiMnGa$ [42] possess sufficiently low magnetostriction coefficients of about $\lambda_s \approx$ 2–10 μm m^{-1} to be classified as vanishing-magnetostriction materials, but their coercivities $H_c = 1.6$–2.4 kA m^{-1} are too large to be classified also as magnetically soft. The four-component $Al_xFeCoNi$ and $CoFeNiSi_x$ medium-entropy alloys (MEAs) [43] possess low magnetostriction coefficients, which are for most compositions in the range $\lambda_s = 7$–30 μm m^{-1} that is outside of the "supersilence" limit. An exception in the $CoFeNiSi_{0.25}$ composition, which possesses low enough $\lambda_s \approx 2.5$ μm m^{-1} and coercivity $H_c \approx 400$ A m^{-1} to classify as a supersilent MEA material. The $(Fe_{0.3}Co_{0.5}Ni_{0.2})_{100-x}(Al_{1/3}Si_{2/3})_x$ HEAs [44] possess $\lambda_s > 8$ μm m^{-1}, which is too high to be classified as vanishing-magnetostriction materials. To the best of our knowledge, the $(GaNi)_xCoCrFe$ HEAs (together with the $AlCoFeNiCu_x$ HEAs) exhibit the best supersilent characteristics of all five-component alloys investigated to date.

Currently, the class of supersilent ferromagnetic HEAs comprises only two members, the $AlCoFeNiCu_x$ ($x = 2.0$–3.0) and the $(GaNi)_x$-$CoCrFe$ ($x = 0.4$–1.6) systems. Regarding the microscopic origin of the smart combination of magnetic softness and vanishing magnetostriction, there emerges a questions whether these two systems are identical, so that $(GaNi)_xCoCrFe$ is just another variant of the $AlCoFeNiCu_x$, or there are some fundamental physical differences between them. The origin of magnetic softness, which is the phenomenon of exchange averaging of magnetic anisotropy, is the same for both systems, while the origin of vanishing magnetostriction is different. In the $AlCoFeNiCu_x$, it is a result of compensation of magnetostrictions of opposite signs of the two present ferromagnetic phases [5], whereas in the $(GaNi)_xCoCrFe$, it originates from the nanostructured morphology of a single ferromagnetic phase. There thus exists a fundamental difference between the $AlCoFeNiCu_x$ and the $(GaNi)_xCoCrFe$ multi-phase HEA systems.

CRediT authorship contribution statement

Jože Luzar: Investigation, Formal analysis. **Andreja Jelen:** Validation, Investigation. **Juraj Nálepka:** Investigation, Formal analysis. **Saeid Salari:** Investigation, Formal analysis. **Primož Koželj:** Writing – review & editing, Visualization, Supervision, Methodology, Investigation, Formal analysis. **Stanislav Vrtnik:** Writing – review & editing, Supervision, Methodology, Investigation, Funding acquisition, Formal analysis. **Peter Mihor:** Investigation, Data curation. **Julia Petrović:** Validation, Investigation, Formal analysis. **Magdalena Wencka:** Writing – review & editing, Validation, Investigation. **Goran Dražić:** Writing – review & editing, Methodology, Investigation, Formal analysis. **Anton Meden:** Writing – review & editing, Methodology, Investigation. **Pavol Priputen:** Writing – review & editing, Supervision, Resources, Methodology, Investigation, Funding acquisition, Conceptualization. **Janez Dolinšek:** Writing – review & editing, Writing – original draft, Validation, Methodology, Funding acquisition, Formal analysis, Conceptualization.

Declaration of competing interest

The authors declare that they have no known competing financial interests or personal relationships that could have appeared to influence the work reported in this paper.

Acknowledgements

The Slovenian authors acknowledge the financial support from the Slovenian Research and Innovation Agency (Research Core Funding No. P1-0125 and Project No. N1-0330). The Slovak authors acknowledge the financial support from the Slovak Research and Development Agency,

grant No. APVV-20-0124, and the Scientific Grant Agency VEGA, grant No. 1/0692/22. J.D. is grateful to Dr. Natalia F. Shkodich from the University of Duisburg-Essen, for acquainting him with the atom probe tomography (APT) results on the CoCrFeNiGa alloy prior to publication.

Appendix A. Supplementary data

Supplementary data to this article can be found online at https://doi.org/10.1016/j.matdes.2024.113396.

Data availability

Data will be made available on request.

References

[1] Y. Zhang, History of high-entropy materials, in: High-Entropy Materials: A Brief Introduction, Springer, Singapore, 2019, pp. 1–33.
[2] Z. Li, K.G. Pradeep, Y. Deng, D. Raabe, C.C. Tasan, Metastable high-entropy dual-phase alloys overcome the strength-ductility trade-off, Nature 534 (2016) 227–230.
[3] P. Koželj, S. Vrtnik, A. Jelen, M. Krnel, D. Gačnik, G. Dražić, A. Meden, M. Wencka, D. Jezeršek, J. Leskovec, S. Maiti, W. Steurer, J. Dolinšek, Discovery of a FeCoNiPdCu high-entropy alloy with excellent magnetic softness, Adv. Eng. Mater. 21 (2019) 1801055.
[4] J.M.D. Coey, in: Magnetism and Magnetic Materials, Cambridge University Press, Cambridge, 2010, pp. 299–301.
[5] J. Luzar, P. Priputen, M. Drienovský, S. Vrtnik, P. Koželj, A. Jelen, M. Wencka, D. Gačnik, P. Mihor, B. Ambrožič, G. Dražić, A. Meden, J. Dolinšek, Zero-magnetostriction magnetically soft high-entropy alloys in the $AlCoFeNiCu_x$ (x = 0.6–3.0) system for supersilent applications, Adv. Mater. Interfaces 9 (2022) 2201535.
[6] A. Goldman, Magnetic Components for Power Electronics, Kluwer, Dordrecht, 2002.
[7] D. Azuma, R. Hasegawa, Audible noise from amorphous metal and silicon steel-based transformer core, IEEE Trans. Magn. 44 (2008) 4104–4106.
[8] P. Zhang, L. Li, Vibration and noise characteristics of high-frequency amorphous transformer under sinusoidal and non-sinusoidal voltage excitation, Int. J. Electr. Power Energy Syst. 123 (2020) 106298.
[9] See, e.g. B.S. Murthy, J.-W. Yeh, S. Ranganathan, High-Entropy Alloys, Elsevier, Amsterdam, 2014, pp. 191–204.
[10] A. Takeuchi, A. Inoue, Classification of bulk metallic glasses by atomic size difference, heat of mixing and period of constituent elements and its application to characterization of the main alloying element, Mater. Trans. 46 (2005) 2817–2829.
[11] N. Shkodich, F. Staab, M. Spasova, K.V. Kuskov, K. Durst, M. Farle, Effect of high-pressure torsion on the microstructure and magnetic properties of nanocrystalline $CoCrFeNiGa_x$ (x = 0.5, 1.0) high entropy alloys, Materials 15 (2022) 7214.
[12] S.-M. Na, J.-H. Yoo, P.K. Lambert, N.J. Jones, Room-temperature ferromagnetic transitions and the temperature dependence of magnetic behaviors in FeCoNiCr-based high-entropy alloys, AIP Adv. 8 (2018) 056412.
[13] F.R. de Boer, R. Boom, W.C.M. Mattens, A.R. Miedema, A.K. Niessen, Cohesion in Metals: Transition Metal Alloys (Cohesion and Structure), North Holland, Amsterdam, 1988.
[14] J.M.D. Coey, Magnetism and Magnetic Materials (ref. [4]), pp. 449–450.
[15] K.H.J. Buschow, F.R. de Boer, in: Physics of Magnetism and Magnetic Materials, Springer, Boston, MA, 2003, pp. 147–163.
[16] D.V. Chashin, D.A. Burdin, L.Y. Fetisov, N.A. Economov, Y.K. Fetisov, Precise measurements of magnetostriction of ferromagnetic plates, J. Sib. Fed. Univ. – Math. Phys. 11 (2018) 30–34.
[17] A. del Moral, Handbook of Magnetostriction and Magnetostrictive Materials, vol. 1–2, Del Moral, Zaragoza, 2008.
[18] J.M.D. Coey, Magnetism and Magnetic Materials (ref. [4]), pp. 209–218.
[19] O. Schneeweiss, M. Friák, M. Dudová, D. Holec, M. Šob, D. Kriegner, V. Holý, P. Beran, E.P. George, J. Neugebauer, et al., Magnetic properties of the CrMnFeCoNi high-entropy alloy, Phys. Rev. B 96 (2017) 014437.
[20] Y. Zhang, T. Zuo, Y. Cheng, P.K. Liaw, High-entropy alloys with high saturation magnetization, electrical resistivity and malleability, Sci. Rep. 3 (2013) 1455.
[21] F. Tian, L.K. Varga, N. Chen, L. Delczeg, L. Vitos, *Ab initio* investigation of high-entropy alloys of 3*d* elements, Phys. Rev. B 87 (2013) 075144.
[22] D. Ma, B. Grabowski, F. Koermann, J. Neugebauer, D. Raabe, *Ab initio* thermodynamics of the CoCrFeMnNi high entropy alloy: importance of entropy contributions beyond the configurational one, Acta Mater. 100 (2015) 90–97.
[23] Z. Dong, S. Schönecker, W. Li, D. Chen, L. Vitos, Thermal spin fluctuations in CoCrFeMnNi high entropy alloy, Sci. Rep. 8 (2018) 12211.
[24] H. Kaneko, M. Homma, K. Nakamura, M. Okada, G. Thomas, Phase diagram of Fe–Cr–Co permanent magnet system, IEEE Trans. Mag. MAG-13 (1977) 1352.
[25] M. Okada, G. Thomas, M. Homma, H. Kaneko, Microstructure and magnetic properties of Fe–Cr–Co alloys, IEEE Trans. Magn. MAG-14 (1978) 245–252.
[26] S. Jin, G.Y. Chin, Fe-Cr-Co magnets, IEEE Trans. Magn. MAG-23 (1987) 3187–3192.
[27] Z. Xiang, L. Zhang, Y. Xin, B. An, R. Niu, M. Mardani, T. Siegrist, J. Lu, R. E. Goddard, T. Man, et al., Ultrafine microstructure and hardness in Fe-Cr-Co alloy induced by spinodal decomposition under magnetic field, Mater. Des. 199 (2021) 109383.
[28] M. Feuerbacher, Dislocations and deformation microstructure in a B2-ordered $Al_{28}Co_{20}Cr_{11}Fe_{15}Ni_{26}$ high-entropy alloy, Sci. Rep. 6 (2016) 29700.
[29] P. Koželj, A. Jelen, G. Dražić, S. Vrtnik, J. Luzar, M. Wencka, A. Meden, M. Feuerbacher, J. Dolinšek, Complex magnetism of single-crystalline AlCoCrFeNi nanocomposite high-entropy alloy, iScience 26 (2023) 106894.
[30] See, e.g., K. Binder, A.P. Young, Spin Glasses: Experimental Facts, Theoretical Concepts, and Open Questions, Rev. Mod. Phys. 58 (1986) 801–976.
[31] J.A. Mydosh, in: Spin Glasses: An Experimental Introduction, Taylor & Francis, London, 1993, p. 67.
[32] M.H. Tsai, Physical properties of high entropy alloys, Entropy 15 (2013) 5338–5345.
[33] See, for a review, B.S. Murthy, J.W. Yeh, S. Ranganathan, High-Entropy Alloys (ref. [9]), pp. 154–155.
[34] See, for a review, J.-W. Yeh, S.-K. Chen, H.C. Shih, Y. Zhang, T.T. Zuo, Functional properties, in: M.C. Gao, J.-W. Yeh, P.K. Liaw, Y. Zhang (Eds.), High-Entropy Alloys: Fundamentals and Applications, Springer International Publishing Switzerland, Switzerland, 2016, pp. 243–248.
[35] L. Han, Z. Rao, I.R. Souza Filho, F. Maccari, Y. Wei, G. Wu, A. Ahmadian, X. Zhou, O. Gutfleisch, D. Ponge, D. Raabe, Z. Li, Ultrastrong and ductile soft magnetic high-entropy alloys via coherent ordered nanoprecipitates, Adv. Mater. 33 (2021) 2102139.
[36] L. Han, F. Maccari, I.R. Souza Filho, N.J. Peter, Y. Wei, B. Gault, O. Gutfleisch, Z. Li, D. Raabe, A mechanically strong and ductile soft magnet with extremely low coercivity, Nature 608 (2022) 310–316.
[37] M. Harivandi, M. Malekan, S.A. Seyyed Ebrahimi, Soft magnetic high entropy alloy with excellent ductility and high electrical resistance, Met. Mater. Int. 28 (2022) 556–564.
[38] P. Kumari, A.K. Gupta, R.K. Mishra, M.S. Ahmad, R.R. Shahi, A comprehensive review: recent progress on magnetic high entropy alloys and oxides, J. Magn. Magn. Mater. 554 (2022) 169142.
[39] D. Jiang, Z. Yuan, Z. Zhu, M. Yao, NiCoCrFeY high entropy alloy nanopowders and their soft magnetic properties, Materials 17 (2024) 534.
[40] W. Gao, Y. Dong, X. Jia, L. Yang, X. Li, S. Wu, R. Zhao, H. Wu, Q. Li, A. He, J. Li, Novel CoFeAlMn high-entropy alloys with excellent soft magnetic properties and high thermal stability, J. Mater. Sci. Technol. 153 (2023) 22–31.
[41] J. Zhu, M. Lv, C. Liu, X. Tan, H. Xu, Effect of neodymium and yttrium addition on microstructure and DC soft magnetic property of dual-phase FeCoNi(CuAl)0.8 high-entropy alloy, J. Rare Earth 41 (2023) 1562–1567.
[42] T.T. Zuo, M. Zhang, P.K. Liaw, Y. Zhang, Novel high entropy alloys of $Fe_xCo_{1-x}NiMnGa$ with excellent soft magnetic properties, Intermetallics 100 (2018) 1–8.
[43] T.T. Zuo, R.B. Li, X.J. Ren, Y. Zhang, Effects of Al and Si addition on the structure and properties of CoFeNi equal atomic ratio alloy, J. Magn. Magn. Mater. 371 (2014) 60–68.
[44] Y. Zhang, M. Zhang, D. Li, T. Zuo, K. Zhou, M.C. Gao, B. Sun, T. Shen, Compositional design of soft magnetic high entropy alloys by minimizing magnetostriction coefficient in $(Fe_{0.3}Co_{0.5}Ni_{0.2})_{100-x}(Al_{1/3}Si_{2/3})_x$ system, Metals 9 (2019) 382.